predominantly associated with transverse single spin modes, $S^{\perp}$ and S^{z}, as well as longitudinal two-spin correlation functions, $S^{\parallel}S^{\parallel}$. This is in agreement with previous studies that interpreted the A excitation as a composite excitation of longitudinal (Higgs) two-particle and transverse bimagnon modes [60, 61]. Thus, the modes at around 80 meV have a multiparticle spin character and are accessible by both single transverse and double longitudinal spin excitations. Additionally, it can be seen from the calculation that the lowest-energy excitations lie at around 20 and 40 meV. The single spin flip mode at 40 meV is also active in the RIXS process, but could not be observed experimentally due to the limitation in energy resolution.

For $Ca_3Ru_2O_7$ in the right panels, different observations can be made. Although the A excitation can also be associated with magnetic excitations, it lies at slightly lower energies and has a predominant transverse character of both single $S^{\perp}$ and S^{z} modes and two-particle $S^{\perp}S^{\perp}$ modes. Interestingly, the simulation also predicts a noticeable shift in energy of about 20-30 meV when going from $\boldsymbol{q} = (0, 0)$ to $(\pi, 0)$. this bandwidth is in good agreement with the observed dispersion for this excitation. Moreover, the orbital angular momentum correlation functions reveal that the A excitation in Ca_2RuO_4 has a significant orbital contribution. However, these orbital contributions are suppressed in $Ca_3Ru_2O_7$. This is in agreement with the difference in orbital occupation and the fact that in $Ca_3Ru_2O_7$, the doublon tends to occupy different orbitals on neighbouring ruthenium atoms. Additionally, in $Ca_3Ru_2O_7$, the spin–orbit coupling aligns the orbital moments, since there is a ferromagnetic spin coupling. Together, this implies that orbital variations are suppressed in the low-energy spin sector. It can therefore be argued that the suppression of orbital components in this excitation allows for a larger effective exchange, which in turn allows for a larger effective bandwidth.

3.3.4 Conclusions

In 4*d* TMO systems, comparable energy scales like the Hund's coupling, crystal-field splitting and spin–orbit coupling lead to unconventional magnetic and electronic properties. In particular, the spin–orbit coupling, which entangles the electron spin with the spatial distribution of the electronic cloud in the crystal, makes the electronic states extremely sensitive to intersite connectivity and therefore to the effective dimensionality of the crystal lattice. This is beautifully demonstrated by the combined oxygen K-edge XAS and RIXS study on $Ca_3Ru_2O_7$ and Ca_2RuO_4 presented in this chapter. The comparison of new data on $Ca_3Ru_2O_7$ to the corresponding data on Ca_2RuO_4 reveals how the ground-state fingerprints, the change in dimensionality and in-plane magnetic order, are encoded in the excitation spectra, which are fundamentally different in the two compounds. Whereas the Ca_2RuO_4 spectra

also contain excitations linked to the Mott insulating ground states, the spectra of $Ca_3Ru_2O_7$ only contain the two lowest-energy intra-t_{2g} excitations that do not directly involve the Coulomb interaction. The main observation is the difference in the lowest-lying excitation, which exhibits a strong dispersion in $Ca_3Ru_2O_7$, revealing its collective origin. Supported by the comparison to spin correlation functions, this excitation can be assigned to a transverse mode with multiparticle character. In Ca_2RuO_4 on the other hand, this excitation does not show a strong dispersion with the current resolution, and its nature is a composite longitudinal amplitude and transverse spin mode. In summary, the differences in the excitation spectra of $Ca_3Ru_2O_7$ and Ca_2RuO_4 are well reproduced in the local cluster modelling that takes into account the fundamentally different magnetic ground states.

The presented results prove the capability of oxygen K-edge RIXS in probing the complex electronic structure of $4d$ ruthenates. It was possible to show that modest spin–orbit coupling is the key element that explains the nature of the low-energy excitations and the activation in the RIXS cross-section. In contrast to previous beliefs, it is not necessary to have a strong spin–orbit coupling for spin–orbital excitations to be detectable at the oxygen K-edge. These excitations reveal a fragile balance between competing energy scales and are therefore vital to understanding the emergent phases.

As predicted by the model calculations, excitations at 40 meV are expected to be present in the RIXS spectrum of Ca_2RuO_4. Due to the limited energy resolution, these excitations could not be measured in this or previous studies. However, an improvement in RIXS instrumentation resulting in better resolution has recently been achieved. The next section follows up on this.

3.4 Resolving the Orbital Character of Low-Energy Excitations in Mott Insulator with Intermediate Spin–Orbit Coupling

Experimental sciences always strive to improve resolving power. From astronomy to biology, this is often how new discoveries are made. In condensed matter physics, momentum-resolved spectroscopy techniques are among the most powerful, and improving their resolving power almost always leads to new findings and insights. For example, progress on the RIXS resolving power has allowed experimentalists to tackle important problems such as spin excitations in high-temperature superconductors and lattice vibrations in battery materials [88]. RIXS has also been applied to study fundamental excitations of multi-band Mott insulators with strong spin–orbit

coupling [89, 90, 91]. Many of these studies are, however, still limited by resolving power. In the last chapter, it was seen that theoretical modelling of the RIXS spectra allowed for an estimation of the relative strength of crystal-field splitting and spin–orbit coupling, but the modest value of the spin–orbit coupling is imprinted in the fine structure of the 350 meV excitation sector, leading this sector to be split into four distinct energy levels; see supplemental material in Ref. [72]. This fine structure, as well as a spin excitation predicted by the model around 40 meV, could not previously be resolved due to limitations in energy resolution.

This section presents a state-of-the-art high-resolution oxygen K-edge RIXS study on Ca_2RuO_4, which provides further insight into the complex spin–orbital excitation sector [48].

3.4.1 Methods

The same crystal growth and preparation procedures as for the previous studies were adopted: see section 3.3.1. The only difference was the glueing procedure for the crystals to the sample holder plates, required because Ca_2RuO_4 undergoes a structural transition at 356 K. Heating above this transition with subsequent cooling down in the curing procedure for the glue would result in the destruction of the crystal. Therefore, the Ca_2RuO_4 crystals were glued using EPO-TEK E4110 silver epoxy to ensure thermal and electrical contact to the cryo-manipulator. This silver epoxy can be cured at lower temperatures, i.e. overnight at 70 °C. The XAS and RIXS measurements were carried out at the high-resolution I21 beamline at the Diamond Light Source, UK [25]. At this beamline, the scattering angle γ was fixed to 154°. Analogously to the previous experiments, the in-plane momentum component was varied by changing the incidence angle θ, and the reciprocal space is indexed using the Miller indices in tetragonal notation (h, k, l). The overall energy resolution at the oxygen K-edge was 25 meV (FWHM), which is less than half the value achieved in previous RIXS studies [47, 72]. To determine the zero energy-loss position in the spectra, the energy-gain side of the elastic peak was fitted to a Voigt profile with width fixed to the energy resolution.

3.4.2 Results

Figure 3.11 shows an overview of the RIXS spectra measured on Ca_2RuO_4 at different absorption resonances, which are highlighted in the XAS spectra shown in panel a. At lower energies, indicated by orange and red dashed lines, are the apical and planar resonances hybridized with ruthenium t_{2g} states, as seen earlier. At higher

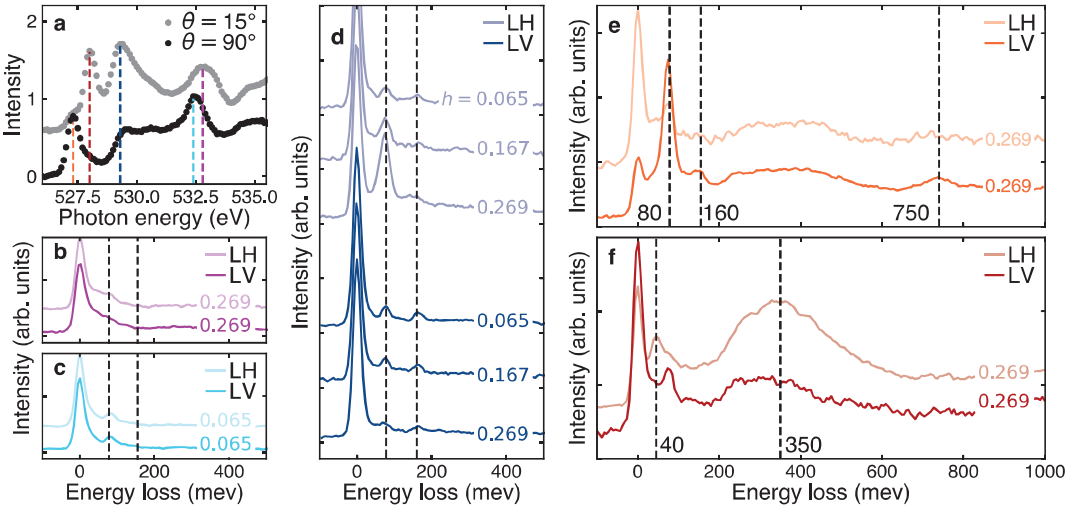

Figure 3.11: High-resolution XAS and RIXS on Ca_2RuO_4. **a** XAS at the oxygen K-edge recorded with LH polarized light. Dashed coloured vertical lines indicate the absorption resonances where RIXS spectra were recorded in **b-f**. **b-d** RIXS spectra at the e_g resonances. **e, f** RIXS spectra at the t_{2g} resonances. Vertical dashed lines in **b-f** indicate the excitations, labelled with their approximate energy scales: 40, 80, 160, 350 and 750 meV.

energies follow the e_g resonances, of which the most intense are highlighted with dark blue, light blue and purple lines. The corresponding RIXS spectra in panels b-f show wonderfully how the better energy resolution in this experiment allows for the detection of additional fine structure in the complex excitation spectra of Ca_2RuO_4.

In total, five distinct low-energy excitations can be detected below 1 eV; they are labelled with their approximate energy scales in panels e and f, to avoid confusion with the earlier studies: 40, 80 (previously A), 160, 350 (previously B) and 750 meV. Furthermore, it is evident that the 80 and 160 meV excitations can be detected through both t_{2g} and e_g resonances. Comparing these results to previous RIXS studies, it can be noted that the 40 and 160 meV excitations are reported here for the first time. The energy scale of the 40 meV excitation matches the magnetic amplitude mode that has been reported by neutron scattering [60]. From the RIXS spectra, however, it can be observed that the 40, 80 and 160 meV excitations appear with a doubling of the energy scale and are observed for the same experimental conditions. This might hint towards a common origin of these excitations.

With the high resolution, it is now also possible to infer more information about the 350 meV excitation sector. Previously, this excitation was only detectable as one single broad peak. From the spectrum recorded with LH polarization in Fig. 3.11f,

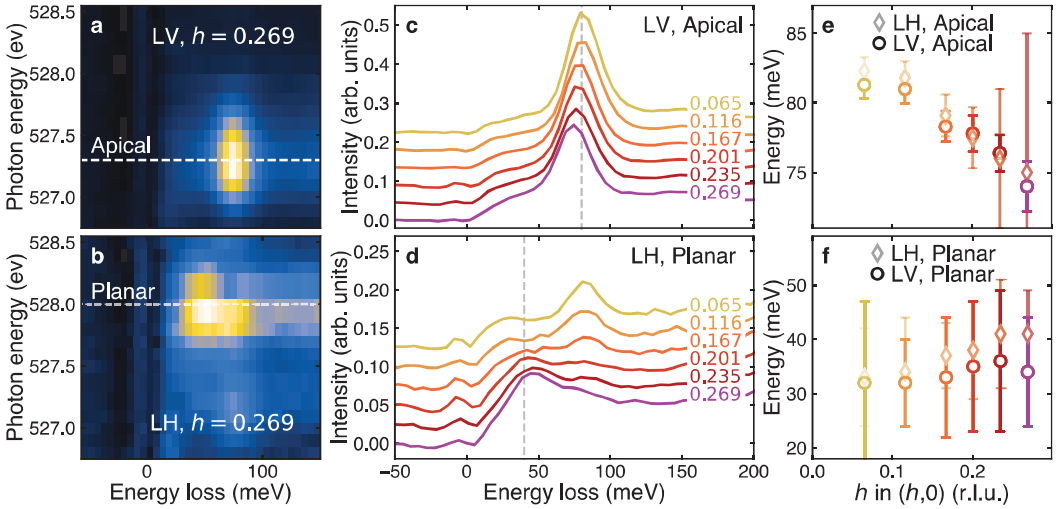

Figure 3.12: Low-energy excitations and their dispersion. a, b RIXS spectra with elastic scattering subtracted as a function of incident photon energy, for light polarizations and momentum transfers as indicated. **c, d** RIXS spectra with elastic scattering subtracted for different momentum transfers as indicated. Vertical dashed lines are guides to the eye for excitations at around 40 and 80 meV. **e, f** Excitation peak position as a function of in-plane momentum transfer h for the 40 (**f**) and 80 meV (**e**) excitations. Error bars reflect standard deviation 3σ from fitting.

it is clear that this block has at least three components, visible as a main peak and distinct shoulders on each side.

Furthermore, a momentum dependence analysis of the two lowest excitations at 40 and 80 meV, after subtraction of elastic scattering, is shown in Fig. 3.12. The 80 meV excitation is most pronounced when probed with LV polarization at the apical resonance, while the 40 meV excitation is most clearly observed with LH polarization at the planar resonance for high in-plane momentum transfers h; see Fig. 3.12a-d. Interestingly, at this light polarization and absorption resonance, the momentum change from the zone centre towards the zone boundary reveals a spectral weight transfer from the 80 meV to the 40 meV excitation, shown in Fig. 3.12d. This is clearly a hint of different orbital and dispersive characters. Tracking the energy as a function of in-plane momentum in panels e and f reveals pronounced differences. The 80 meV excitation disperses rapidly to lower energies upon increased momentum, which has not been observed previously. For the 40 meV excitation, on the other hand, no significant dispersion can be resolved with the energy resolution applied here. The fast dispersion of the 80 meV excitation resembles the one observed in $Ca_3Ru_2O_7$, where the energy shifts around 10 meV within a quarter of the Brillouin zone. However, whereas in $Ca_3Ru_2O_7$, the steepest dispersion is found close to the zone centre, the excitation in Ca_2RuO_4 seems to follow the opposite trend, with a

flat dispersion near the zone centre and then increasing dispersion towards the zone boundary.

3.4.3 Interpretation and Discussion

First, the splitting of the energy levels in the 350 meV sector is discussed. The theoretical modelling described in the supplemental material of Ref. [72] predicts the splitting of this excitation sector due to spin–orbit coupling into four different energy levels. With this model, it can be shown that the RIXS process conserves spin because of the absence of spin–orbit coupling in the intermediate state. Transitions into the lowest of these four levels at the oxygen K-edge RIXS process are mostly not allowed, since they correspond to $\Delta S_z = \pm 1$. Apparently, the only dipole-allowed atomic transitions to the lowest level have negligible amplitudes and are therefore not seen in the RIXS spectrum. The three observed components correspond, therefore, to transitions to the three higher levels in this excitation block. Their excitation energies can be written as a function of crystal-field splitting δ and spin–orbit coupling λ:

$$\begin{aligned} E_1 &= \sqrt{\delta^2 - 2\delta\lambda + 9\lambda^2} \\ E_2 &= 1/2\left(\lambda + \sqrt{\delta^2 + 4\lambda^2} + \sqrt{\delta^2 - 2\delta\lambda + 9\lambda^2}\right) \\ E_3 &= 1/2\left(\delta + 3\lambda + \sqrt{\delta^2 - 2\delta\lambda + 9\lambda^2}\right) \end{aligned} \tag{3.2}$$

From the spectra, the precise energy levels for the 40 meV excitation and the middle level E_2 of the 350 meV excitation can be extracted as 37 meV and 340 meV, respectively. These two energies are marked in Fig. 3.13 with vertical dashed lines. The theoretical model and Eq. (3.2), together with these two energy levels, allow for the calculation of the crystal-field splitting $\delta = 250$ meV and spin–orbit coupling $\lambda = 85$ meV. For a self-consistency check, these two energy scales can be inserted back into Eq. (3.2) to calculate the other two energy levels. These are illustrated by light blue vertical dashed lines in Fig. 3.13. The predicted values agree closely with the observed shoulders to the main excitation peak around 350 meV. Thus, performing this procedure on the high-resolution data allows for a more accurate extraction of the crystal-field splitting and spin–orbit coupling scales.

Next, the two low-energy excitations and their interpretation are discussed. As shown in the previous chapter, the 40 meV excitation has been predicted to be accessible through oxygen K-edge RIXS. Additionally, with inelastic neutron scattering, a dispersive Higgs (amplitude) mode was reported at a similar energy scale [60]. Now, the excitation has been measured with RIXS for the first time, thanks to the improvement in energy resolution. It also has to be stressed that the 40, 80 and

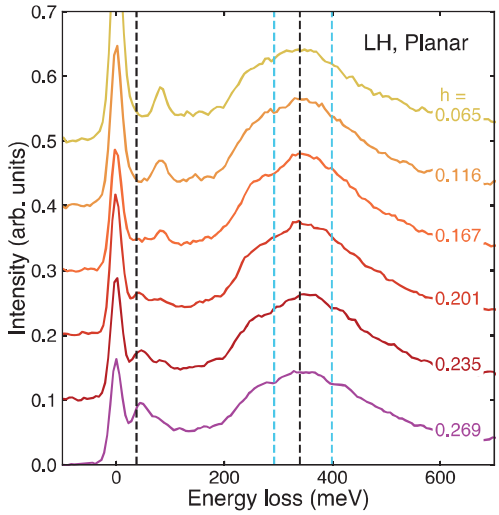

Figure 3.13: Energy level splitting due to spin–orbit coupling. RIXS spectra focusing on the excitation around 350 meV for different momentum transfers as indicated. Black vertical dashed lines indicate the excitation energies extracted from the data used to calculate the crystal-field splitting and spin–orbit coupling. Light blue vertical dashed lines represent the excitation energies obtained with the theoretical model.

160 meV excitations have doubling energy scales, which suggests a connection between their origins. Nevertheless, a possible phononic nature, especially for the 80 meV excitation, needs to be discussed and excluded before moving to the discussion of the spin–orbital origin for the low-energy excitations.

In many oxide compounds, optical phonons have been observed in the energy range from 60-90 meV, for example in $SrTiO_3$ [92] and $La_{1.675}Eu_{0.2}Sr_{0.125}CuO_4$ [93]. Indeed, a Raman spectroscopy study observed a phonon mode just below 80 meV in Ca_2RuO_4 [61]. From the dispersion data presented in this study, however, the 80 meV excitation energy exceeds 80 meV at the zone centre. In addition to this indication against a phononic origin of this excitation, the same arguments made for the A excitation in $Ca_3Ru_2O_7$ in section 3.3.3 can be applied here: the strong dispersion is atypical for optical phonons. The last indication against a phononic nature is based on the electron–phonon coupling and higher-order modes. For phonons to be detectable by RIXS, a strong electron–phonon coupling is required, which in turn leads to relatively intense multiple-phonon excitations. In this case, the 80 meV feature is particularly strong in the RIXS spectrum, hinting towards a large electron–phonon coupling. The two-phonon mode would then be the 160 meV feature. However, the intensity ratio of these two peaks does not suggest a strong electron–phonon coupling [94], leading to contradictory conclusions. Based on these three arguments, a phononic nature for the low-energy excitations can be excluded.

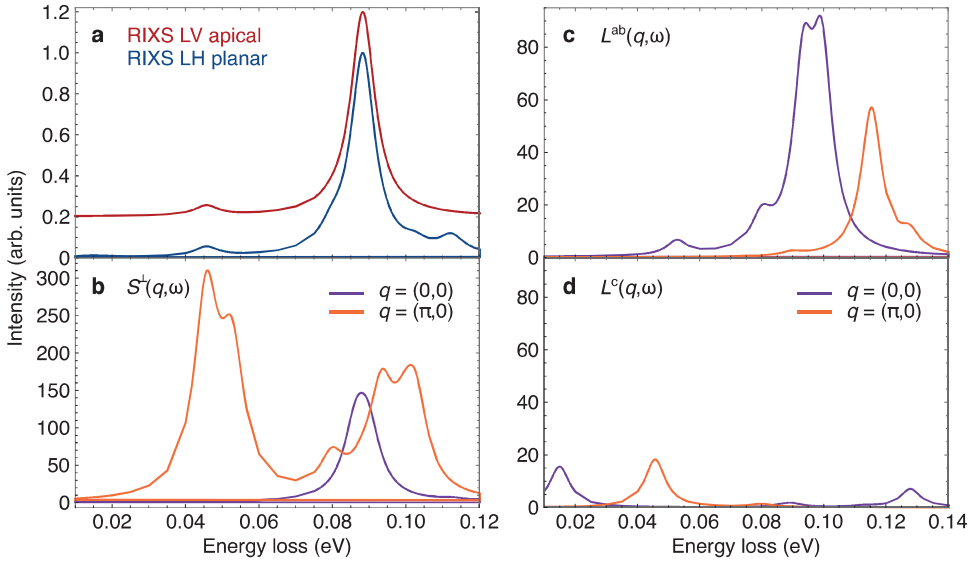

Figure 3.14: Theoretical model calculations. **a** Calculated RIXS spectra at $q = (0, 0)$ for LH planar and LV apical resonances. The spectra were broadened with a 4 meV FWHM Gaussian. **b** Dynamical spin structure factor $S^{\perp}(q, \omega)$ with ruthenium spin momentum orthogonal to the magnetic easy axis. **c** Dynamical orbital angular momentum structure factor $L^{ab}(q, \omega)$ in the ab-plane. **d** Dynamical orbital angular momentum structure factor $L^{c}(q, \omega)$ with orbital angular momentum out-of-plane. Figure adapted from Ref. [48].

To explore the spin–orbital origin of the low-energy excitations instead, the theoretical model adopted in previous studies [47, 72] was extended to a cluster containing two apical oxygens (O_a), one central planar oxygen (O_p) and two ruthenium atoms, having the structure: O_a - Ru - O_p - Ru - O_a. The calculated RIXS spectra for two different experimental geometries, LH planar and LV apical resonances, are shown in Fig. 3.14a. It can be confirmed that both the 40 and 80 meV features can be accessed at both the apical and planar oxygen sites. The magnetic origin of these excitations is confirmed when the dynamical spin response $S(q, \omega)$ (see also section 3.3.3) is taken into account for the extended cluster shown in Fig. 3.14b. The modes at 80 meV are composite magnetic excitations with dominant transverse character, originating from multiple spin modes. This observation is consistent with the previous analysis on a smaller cluster size; see the previous section and Ref. [72]. The 40 meV mode is also composed of transverse spin modes, resulting from the $S^{\perp}$ correlation function. In particular, this mode is observed for $q = (\pi, 0)$, which has a non-trivial phase factor between neighbouring ruthenium sites. This nonlocal spin excitation is observable through both oxygen resonances because of the rotation of the octahedra in the crystal lattice.

The orbital character of the low-energy excitations can be inferred from the calculation

of the dynamical orbital structure factor $L(q, \omega)$. The in-plane (longitudinal) and out-of-plane (transverse) orbital correlation responses are shown in Fig. 3.14c and d, respectively. Again, the momenta $q = (0, 0)$ and $q = (\pi, 0)$ correspond to equal and opposite phases at the ruthenium sites, respectively. It can be seen that the 80 meV feature is mostly from in-plane orbital excitations, corresponding to a longitudinal variation of the angular momentum, whereas the 40 meV has a predominantly out-of-plane/transverse orbital character. This is in line with the experimental observation of the polarization and momentum dependence of these two features in Fig. 3.12d, where the 80 meV excitation is observed when probed with an electric field polarization lying in-plane, whereas the 40 meV is stronger when probed with a polarization lying out-of-plane. Thus, the polarization direction corresponds to the variation of the orbital polarization at the ruthenium site. With this, the spectral weight transfer from 80 meV to 40 meV when increasing the in-plane momentum can be attributed to the change of the polarization from in-plane to out-of-plane directions.

In general, the excitations in Ca_2RuO_4 have a complex character since the spin–orbit coupling leads to an entangling of the spin and orbital angular momentum. This means that excitations of the spin momentum are concomitant with an orbital response. However, the low-energy excitations analysed here correspond to a variation of the orbital angular momentum, not a change in the occupation of the t_{2g} orbitals. The observation of such a variation using oxygen K-edge RIXS is not trivial, as the hybridization of the ruthenium and oxygen orbitals must be taken into account.

3.4.4 Conclusions

The state-of-the-art high-resolution RIXS study on Ca_2RuO_4 presented here illustrates beautifully how the increasing resolving power is required to disentangle the fundamental excitations emerging from an interplay of competing energy scales. A deeper insight into the low-energy structure of this spin–orbit coupling-driven multiband Mott insulator reveals the 40 meV magnetic excitation previously predicted by model calculations and the strongly dispersive nature of the 80 meV excitation. Additionally, an excitation at 160 meV was detected for the first time. The fine structure of the 350 meV excitation block was resolved to reveal direct insight into the energy levels split by spin–orbitcoupling. Lastly, the 750 meV excitation that was reported using ruthenium L_3-edge measurements [95] is now shown to also be accessible through the oxygen K-edge. This extremely rich low-energy excitation spectrum is a direct consequence of the non-trivial magnetic and orbital ground states in this material. The interplay of spin–orbit coupling and crystal-field potential leads to a magnetic ground state consisting of a quantum superposition of several

components. This peculiar character leads to a wealth of spin–orbital excitations with considerable high-energy excitations.

Additionally, comparison to theoretical modelling on an extended cluster allowed for the understanding of the activation of the spin–orbital excitations at 40 and 80 meV in the RIXS cross section for different absorption resonances and polarizations. Most importantly, the 80 meV mode can be ascribed to in-plane longitudinal variation of the orbital angular momentum, whereas the 40 meV mode has predominant transverse orbital character. This is in full agreement with a spectral weight shift from the 80 meV to the 40 meV feature by going from the zone centre towards the zone boundary, when the photon polarization is associated with a variation of the orbital momentum in the corresponding direction. These insights have been possible due to the high energy resolution and the careful theoretical modelling of the system. Future improvements in resolution will allow for an even deeper understanding, by allowing low-lying excitations to be distinguished. Another possibility is to include a polarization analysis of the scattered photons to gain further insight into the angular momentum changes induced in the system.

Overall, the complex excitation landscape of Ca_2RuO_4 offers a unique playground to explore multiple energy scales relevant in extremely correlated electron systems. The direct determination of these relevant electronic energy scales is essential for developing theoretical concepts in the field of multiband Mott insulators, but extends beyond this area, since most exotic phenomena in quantum materials can be traced back to low energy scales.

4 Charge Order in the La-Based Cuprate Superconductors

In 1986, a new era in superconductivity was born with the discovery of the high-T_C superconductor $La_{2-x}Ba_xCuO_4$ by J.G. Bednorz and K.A. Müller [96]. In this copper oxide perovskite, the superconducting transition was found at 30 K, a new record at that time. This discovery was remarkable, considering what was known about superconductivity, with highly conductive metals being considered the most likely candidates for superconductors. In fact, $La_{2-x}Ba_xCuO_4$ shows very poor conductivity at room temperature, and slight changes in its chemical composition can lead to highly insulating properties. More interestingly, the Bardeen–Cooper–Schrieffer (BCS) theory, which describes the microscopic mechanism in conventional superconductors, failed to fully capture the properties of this new copper oxide superconductor. This was the beginning of the research into so-called unconventional superconductors, and sparked the hope that there was indeed no strict upper limit on the transition temperature. Hence, this started a race in search of materials with even higher transition temperatures and, among others, a series of related copper-based materials was discovered, nowadays known as cuprate high-T_C superconductors (HTSCs). The transition temperatures in this family are generally high and include the current record of 138 K at ambient pressure [97].

The unconventional superconductivity in cuprates has been at the centre of scientific efforts for almost 40 years, and yet many questions remain open. This is mostly because superconductivity emerges from strongly correlated electrons, which lead to a plethora of exotic phases and states of matter surrounding the superconducting dome in the phase diagram. One of the archetypical model systems in the cuprate families is $La_{2-x}Sr_xCuO_4$, which can be tuned from an antiferromagnetic Mott insulator through a superconductor to a Fermi liquid metal by hole doping. In this chapter, the study of yet another phase adjacent to the superconducting dome is presented: the charge-order phase in $La_{2-x}Sr_xCuO_4$ and related compounds. It is based on three manuscripts: "High-temperature charge-stripe correlations in $La_{1.675}Eu_{0.2}Sr_{0.125}CuO_4$" [98] (section 4.2), "Fate of charge order in overdoped La-based cuprates" [99] (section 4.3) and "Charge order lock-in by electron-phonon coupling in $La_{1.675}Eu_{0.2}Sr_{0.125}CuO_4$" [93] (section 4.4). For the first manuscript, I

have obtained co-authorship by participation in the experiments and contribution to discussions and manuscript preparation. For the second manuscript, I took the lead in planning, preparing and executing the experiments, analysed the data and wrote the manuscript with input from the other authors, which is reflected by first authorship. For the third manuscript, I took part in the preparation and execution of the experiments as well as the data analysis, and provided input to the manuscript preparation, which is reflected in an equally contributing second authorship. Before going into the details of these three studies, the $La_{2-x}Sr_xCuO_4$ phase diagram is introduced, and the motivation behind the investigation of charge order is elucidated.

$La_{2-x}Sr_xCuO_4$ belongs to the family of Ruddlesden–Popper layered perovskite crystal structures, which also included the calcium ruthenates discussed in the previous chapter. The undistorted high-temperature tetragonal structure of the parent compound La_2CuO_4 is shown in Fig. 4.1a. As in Ca_2RuO_4, the transition metal, here copper, is surrounded by an octahedra of oxygen atoms, which are connected to form planes that are interleaved by a spacer layer. Electronically, the Cu^{2+} has an electron configuration of $3d^9$, in which 9 valence electrons fill the t_{2g} states fully and the e_g states to 3/4 [100]. The system is dominated by strong electron–electron correlations, i.e. Coulomb repulsion, at the copper site, and the emergent correlation physics can be tuned by charge doping. In contrast to Ca_2RuO_4, in which Sr substitution is isovalent, in $La_{2-x}Sr_xCuO_4$ the Sr substitution in the so-called charge reservoir layers induces charge carriers, more specifically holes, in the CuO_2 planes, which have a strong impact on the macroscopic physical properties of the system. This can be seen in the phase diagram depicted in Fig. 4.1b. Below, a selection of the phases relevant to this study will be briefly introduced. The discussion in this work is far from complete and only touches shallowly on a few of the intriguing and complex phenomena found in this material.

4.1 La-Based Cuprate Phase Diagram

Antiferromagnetic Insulator

The undoped parent compound La_2CuO_4 has an odd number of electrons in its valence shell, but the strong Coulomb repulsion localizes them, which means that hopping between adjacent copper sites is strongly suppressed. This leads to the opening of a 2 eV gap [9]. At the same time, the spin degree of freedom at the copper sites forms a long-range antiferromagnetic order, therefore generating an antiferromagnetic Mott insulator. The starting compound La_2CuO_4 has macroscopic

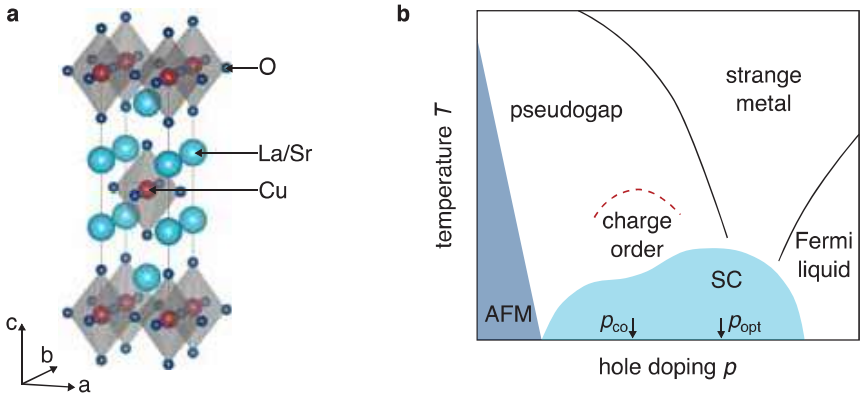

Figure 4.1: $La_{2-x}Sr_xCuO_4$. a Crystal structure of $La_{2-x}Sr_xCuO_4$. **b** Schematic phase diagram of $La_{2-x}Sr_xCuO_4$, showing the antiferromagnetic (AFM) insulating phase, superconductivity (SC), pseudogap, strange metal and Fermi liquid phases. At the charge order doping (p_{co}), the superconducting transition temperature is suppressed due to strong charge order. Here, p_{opt} denotes optimal doping for superconductivity, separating the underdoped ($p < p_{opt}$) from the overdoped ($p > p_{opt}$) regime. Adapted from Ref. [9].

physical properties parallel to Ca_2RuO_4, but the evolution of the phase diagram is profoundly different, as are the underlying microscopic interactions.

Superconductivity

By hole doping, hopping between sites is promoted, which reduces the localization of charge and moves the system away from the insulating phase. Most importantly, at low temperatures a superconducting dome is formed, reaching its maximum transition temperature T_C at the optimal doping p_{opt}. For $La_{2-x}Sr_xCuO_4$, $p_{opt} \approx 0.15$ yields the maximum $T_{C,max} \approx 38\,\mathrm{K}$. For different cuprate families, T_C scales with the number of CuO_2 layers in the crystal structure up to three layers, which means that the single-layer compound has the lowest T_C, while the trilayer shows the highest [43]. In fact, the CuO_2 layers are responsible for superconductivity, as the lowest-energy band structure is composed of the Cu $3d$ and O p bands, which determine the macroscopic electronic properties. The phase is therefore quasi-two-dimensional, especially in the single-layer case. Most importantly, the superconducting state of the cuprates distinguishes itself from conventional superconductors by a d-wave symmetric superconducting wave function. This means that the dependence of the superconducting gap on the momentum exhibits nodes, with the gap at the Fermi level being zero. Thus, the superconducting phase is unconventional and associated with a broken symmetry distinct from BCS conventional superconductors. Despite extensive efforts, the detailed mechanism behind high-temperature superconductivity,

i.e. the interaction behind the Cooper pair formation, has not been established yet.

Pseudogap

Another highly debated and peculiar phase of $La_{2-x}Sr_xCuO_4$ is the pseudogap phase. It manifests in the underdoped to optimally doped region as a spectral gap in the normal (non-superconducting) state. This means that an energy gap opens along certain parts of the underlying Fermi surface, resulting in Fermi arcs. This is in contrast to the superconducting gap state, in which the whole Fermi surface is gapped with the exception of point nodes. The onset temperature T^* has been difficult to track and the origin of this phase has puzzled researchers for decades. Several theories have been put forward. It may be a crossover phenomenon [101], a precursor to a symmetry breaking or emerge through a quantum critical point inside the superconducting dome [102, 103]. The latter scenario raises the question of which symmetry breaks across this point [104, 105, 106]. A recent study of the magnetic ground state with superconductivity suppressed by a strong magnetic field found that the antiferromagnetic spin-glass phase persists up to a doping consistent with the pseudogap critical doping, suggesting a link between the two [107].

Charge Order

Looking closely at the superconducting dome, one can observe that, in the underdoped regime, a suppression of the transition temperature exists at around 1/8 doping. This suppression is related to charge order that was found inside the pseudogap phase and was first explained by Tranquada *et al.* [108] as coupled spin and charge modulations in the form of two-dimensional stripes, which have a commensuration of eight and four lattice units in $La_{2-x}Sr_xCuO_4$, respectively. In general, charge order in cuprates refers to the periodic modulation of the valence electron density in the CuO_2 planes [109]. There are several kinds of charge order found in different compounds. The terminology varies between charge order, charge density wave and charge ordering, depending on the kind of modulation and its driving mechanism. Throughout this work, the term charge order is used to refer broadly to a periodic charge modulation, irrespective of its origin. Since its discovery, charge order has been established in virtually all known hole-underdoped cuprates and seems to be an integral element of the physics of these systems. Because the modulation is usually incompatible with the underlying lattice, translational symmetry is broken. However, different ordering vectors have been observed for different cuprate families [109]. Additionally, the coupling of spin and charge modulations needs to be questioned, as both charge order without spin and spin order without charge have been observed [110, 111]. Another

point of uncertainty is the evolution of charge order above optimal doping and, with this, the interplay of charge order with superconductivity and the pseudogap. A clear onset temperature has not been established either: the dashed line in Fig. 4.1b represents early measurements only. This chapter will present three studies that examine these open questions concerning charge order and its role in the phase diagram of $La_{2-x}Sr_xCuO_4$ and its sister compound $La_{1.8-x}Eu_{0.2}Sr_xCuO_4$.

4.2 High-Temperature Charge-Stripe Correlations in $La_{1.675}Eu_{0.2}Sr_{0.125}CuO_4$

Motivated by of the numerous open questions regarding charge order presented in the last section, this section reports the detection of weaker signals at high temperatures by isolating the elastic scattering stemming from charge order from inelastic contributions. This experimental technique is shown to allow for precise tracking of the charge order signal to temperatures well above the detection threshold for energy-integrating techniques.

The study focuses on $La_{1.675}Eu_{0.2}Sr_{0.125}CuO_4$, which has a low-temperature tetragonal (LTT) crystal structure that appears with charge order. Other compounds that share the LTT structure include $La_{1.475}Nd_{0.4}Sr_{0.125}CuO_4$ and the $La_{2-x}Ba_xCuO_4$ system, which both exhibit long-range spin–charge stripe order concomitant with the LTT phase. Interestingly, in the LTT phase, the CuO_6 octahedra are rotated around the copper–oxygen bond direction, which breaks C_4 symmetry. This symmetry breaking is also consistent with the stripe order. Therefore, the question arises whether the LTT phase in these compounds is a trigger or a consequence of stripe order, especially because the first measurements found the same onset temperature for stripe order and the LTT structure [108, 112]. On the other hand, in $La_{1.875}Ba_{0.125}CuO_4$, experiments found the stripe order even when the LTT phase was suppressed by hydrostatic pressure [113] or temperature [114]. This suggests that charge–stripe order emerges spontaneously outside the LTT phase. So far, this has not been observed for $La_{1.675}Eu_{0.2}Sr_{0.125}CuO_4$, whose LTT phase persists up to $\sim 125\,\mathrm{K}$, thus having the highest LTT onset temperature. For this compound, stripe order has been measured with resonant elastic x-ray scattering only up to 80 K, leaving a large temperature gap between the two phases [115, 116, 117]. Therefore, a unified picture among the La-based cuprates is missing and the connection between the LTT and the charge-order phase remains unclear.

This section presents a copper L_3-edge RIXS study on $La_{1.675}Eu_{0.2}Sr_{0.125}CuO_4$ at the well-known 1/8 doping for charge order, with the charge correlations sensitively

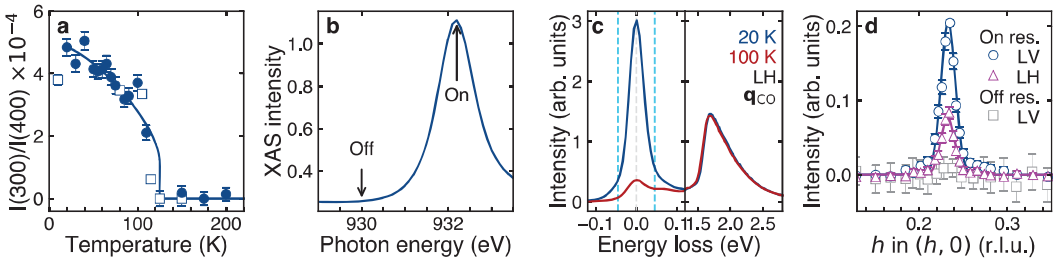

Figure 4.2: LTT phase and charge order in $La_{1.675}Eu_{0.2}Sr_{0.125}CuO_4$. **a** (3,0.0) structural peak normalized by the (4,0,0) Bragg peak as a function of temperature. The filled and open symbols are data measured by counting at peak and background positions or by fitting longitudinal scans, respectively. The solid line is a guide to the eye. **b** XAS spectrum at the Cu L_3 edge recorded at normal incidence with LV polarized light. Arrows indicate photon energies on and off resonance. **c** RIXS spectra recorded with high resolution and LH polarized light near the charge order $\boldsymbol{q}_{\mathrm{CO}}$ at different temperatures. The energy region around elastic scattering and *dd* excitations is shown on different energy scales for clarity. Vertical dashed lines indicate ± FWHM of the energy resolution. **d** Elastic intensity along the in-plane momentum h measured with different light polarizations and with incidence energy tuned to the resonance and off resonance as indicated in **b**. Figure adapted from Ref. [98].

tracked to high temperatures and compared to other La-based cuprates [98].

4.2.1 Methods

The floating zone method was used to grow high-quality single crystals of $La_{1.675}Eu_{0.2}Sr_{0.125}CuO_4$ (LESCO 1/8), $La_{1.475}Nd_{0.4}Sr_{0.125}CuO_4$ (LNSCO 1/8), $La_{1.875}Ba_{0.125}CuO_4$ (LBCO 1/8) and $La_{1.875}Sr_{0.125}CuO_4$ (LSCO 1/8). All crystals were prealigned ex situ using Laue diffraction and cleaved in situ using the top-post technique. The XAS and RIXS measurements were carried out at the ADRESS, I21 and ID32 beamlines; see chapter 2.1.2. For measurements on LESCO, the energy resolution ranged between 45-113 meV FWHM. As in the previous chapter, the in-plane momentum component was varied through the incident light angle θ and the reciprocal space is indexed by Miller indices $(h, k, l) = (q_x a/2\pi, q_y b/2\pi, q_z c/2\pi)$, where $\boldsymbol{q} = (q_x, q_y, q_z)$ is the wave vector or transferred momentum. To access momenta along k, the sample was rotated around azimuthal angle ϕ. Tetragonal lattice parameters were used for LESCO, with $a \approx b \approx 3.79$ Å and $c \approx 13.1$ Å.

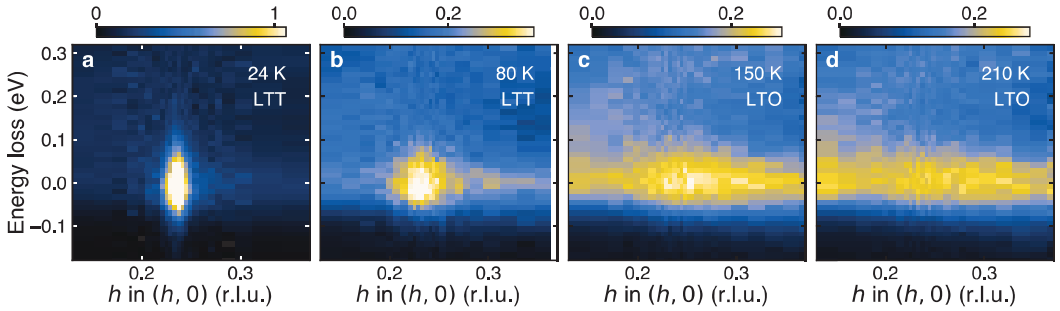

Figure 4.3: Temperature dependence of the charge order. a-d RIXS intensity distribution maps of the raw spectra through the charge order peak at different temperatures as indicated. Figure adapted from Ref. [98].

4.2.2 Results

The onset temperature of the LTT phase in LESCO 1/8 is confirmed by the non-resonant (8.048 keV) x-ray diffraction results shown in Fig. 4.2a. The (3,0,0) Bragg peak is allowed in the LTT phase, but forbidden in the low-temperature orthorhombic (LTO) phase, which follows the LTT phase at higher temperatures. As expected, the intensity of the (3,0,0) peak drops to zero at the transition detected at ~ 125 K.

To follow the charge order as a function of temperature, RIXS was used to sensitively track the elastic scattering signal. For the tuning of the incident photon energy to the Cu L_3-edge, the XAS spectrum is shown in Fig. 4.2b. A single resonance peak is observed around 932.2 eV. The RIXS spectrum recorded at this resonance is shown in Fig. 4.2c, focusing on the elastic and *dd* excitation energy regions for two indicated temperatures. While the *dd* excitations do not change in temperature, the elastic scattering is strongly enhanced at low temperatures, indicative of the charge-order reflection peak. To quantify the charge order at different momenta and temperatures, RIXS spectra taken at different momentum transfers and temperatures can be analysed, and elastic scattering can be inferred by integrating the intensity in an energy window defined by $\pm$ FWHM of the energy resolution around the elastic line. To account for different detection efficiencies at different experimental geometries, the RIXS intensity is normalized first to the integrated spectral weight of the *dd* excitations. With this procedure, the elastic scattering is filtered from the inelastic contributions, which allows the charge order signal to be tracked more accurately, even in a regime where inelastic contributions like the *dd* excitations dominante the spectrum. The following results will show that the resonant energy-resolved detection is much more sensitive to detect weak charge correlations.

Elastic scans recorded in the manner described above are shown in Fig. 4.2d as a function of in-plane momentum transfer h. Elastic scattering peaks strongly for

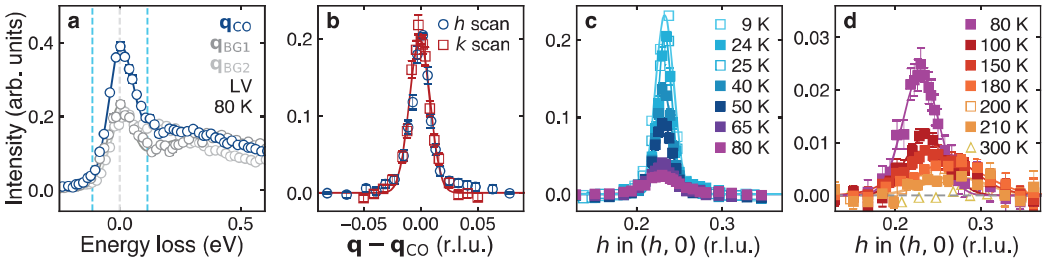

Figure 4.4: Elastic scans through the charge order. **a** RIXS spectra collected at the charge order wave vector $\boldsymbol{q}_{\mathrm{CO}}$ and at two background positions $\boldsymbol{q}_{\mathrm{BG1}} = (0.346, 0)$ and $\boldsymbol{q}_{\mathrm{BG2}} = (0.129, 0)$. Light blue vertical dashed lines indicate the energy window for the elastic intensity integration. **b** Elastic scans along h and k directions. **c, d** Elastic h scans recorded at different temperatures with linear background subtracted. The filled and open markers represent data collected at ADRESS and I21, respectively. Solid lines are Gaussian fits. Figure adapted from Ref. [98].

resonant incident photon energy at a momentum $h = 0.233$ due to the charge order. In fact, charge stripe order, as discussed in the previous section, manifests itself by satellite peaks at $\boldsymbol{q} = \boldsymbol{\tau} + \boldsymbol{q}_{\mathrm{CO}}$, where $\boldsymbol{\tau}$ is a fundamental Bragg reflection peak. The in-plane charge order wave vector $\boldsymbol{q}_{\mathrm{CO}} = (\pm\delta_a, 0)$ and $(0, \pm\delta_b)$ results in four satellite peaks arranged in a cross around the main Bragg peak. The so-called incommensurability $\delta_a = \delta_b = \delta$ is close to 1/4 in La-based cuprates. Therefore, the peak in elastic scattering observed here with RIXS corresponds to one of these satellite peaks with $\delta = 0.233$, consistent with previous reports [116, 118]. From the scans, it can also be seen that the electronic ordering is much stronger if probed on the resonance and with LV light polarization.

The temperature evolution of the charge order is shown in Fig. 4.3a-d, where the raw RIXS spectra are shown in an intensity distribution map along the in-plane momentum h. At low temperatures, the charge order peak is intense and sharp. With increasing temperature, the peak becomes less intense and broader, but is still detectable up to 210 K. Most importantly, the charge correlations persist beyond the onset temperature of 80 K that was previously reported based on resonant elastic x-ray scattering, and also beyond the LTT phase.

The elastic scattering is markedly enhanced when approaching the charge order wave vector $\boldsymbol{q}_{\mathrm{CO}}$, as can be seen in Fig. 4.4a. Furthermore, the longitudinal h and transverse k elastic scans in Fig. 4.4b confirm that the peak is isotropic, suggesting identical correlation lengths in both directions. Therefore, the longitudinal elastic scans in Fig. 4.4c and d were used to extract temperature-dependent information about the charge stripe order in LESCO 1/8. The scans are fitted with a Gaussian lineshape and a linear background to extract the scattering amplitude I, the incommensurability δ defined as the peak position, and the in-plane correlation length ξ defined as the

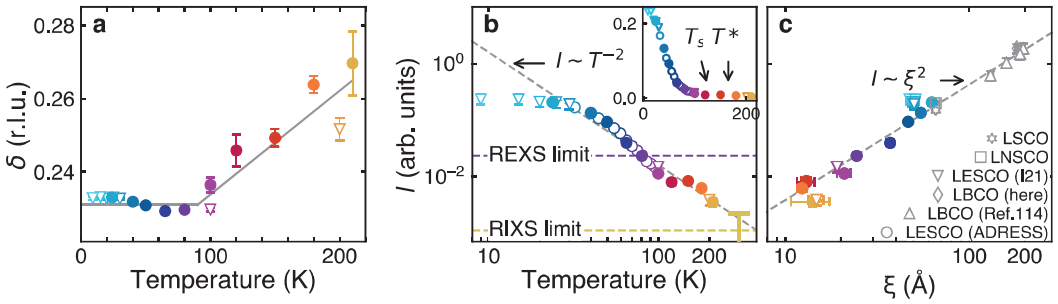

Figure 4.5: Incommensurability, scattering amplitude and correlation length. **a, b** Incommensurability δ and scattering amplitude I of the charge order as a function of temperature. Filled circles and open triangles represent the fitted parameters of h scans collected at ADRESS and I21, respectively. Open circles in **b** represent the mean-background-subtracted elastic scattering intensity measured at $\boldsymbol{q} = (0.235, 0)$ with backgrounds at $\boldsymbol{q} = (0.129, 0)$ and $(0.346, 0)$. The yellow upper error bar at 300 K denotes the upper limit of the peak height estimated from the h scan. The inset shows the data on a linear scale. REXS: resonant elastic x-ray scattering. **c** Charge order scattering amplitude as a function of correlation length ξ for different compounds as indicated. The colors indicate the temperatures for the LESCO 1/8 data as in **a, b**. Scans on LSCO, LNSCO and LBCO can be found in supplemental material of Ref. [98]. Figure adapted from Ref. [98].

inverse half width at half maximum (HWHM). The temperature evolution of these three parameters is displayed in Fig. 4.5.

The first figure panel in this figure shows a constant value for the incommensurability below ~ 80 K and a linear increase above that temperature up to $\delta \approx 0.27$, indicating a lock-in mechanism to $\delta \approx 0.23$ at low temperatures. On the other hand, the scattering or diffraction amplitude decreases very slowly below 30 K, with a sharp drop at higher temperatures. The rapid decrease is approximately described by a T^{-2} power-law decay. The inset of Fig. 4.5b shows no effect of the structural or pseudogap transition temperatures on the diffraction amplitude of charge order. The correlation length ξ, defined by the inverse HWHM, is an indication of how long- or short-range the correlations are in real space. It shows a similar decay to the amplitude, and plotting the amplitude I against the correlation length ξ reveals a simple power law $I \sim \xi^2$. Interestingly, this power law also seems to hold for other compounds in the La-based single-layer cuprate family.

4.2.3 Interpretation and Discussion

The first observation yielded by this study is the persistence of charge correlations up to temperatures well above the previous onset temperature for charge order and also well above the LTT transition temperature. This has not been seen in

previous studies on the charge order due to their lower detection sensitivities. This work shows how the charge order is observed an order of magnitude more intensely at the copper resonance, where the scattering from valence electrons is enhanced. Additionally, RIXS can distinguish between quasi-elastic and inelastic contributions. This is essential when the charge correlation signal is comparable to or weaker than inelastic contributions like the *dd* excitations. The previous onset temperature found by resonant elastic scattering is limited by exactly this dominance of inelastic contributions to the signal. The onset temperature found in those studies, of around 80 K, marks the temperature where the *dd* excitation signal becomes dominant over the charge correlations, so that this is the detection limit for energy-integrating techniques, rather than an intrinsic and fundamental onset temperature. Thus, the differentiation of elastic and inelastic scattering contributions is essential for probing the charge order in LESCO.

The second observation is that the evolution of the incommensurability δ as a function of temperature shows an increase at higher temperatures. However, the temperature at which the incommensurability starts to increase is not related to the LTT onset temperature, indicating no relation between the two. A move of the incommensurability away from 1/4 has also been observed in LBCO at high temperatures [114]. This is noteworthy because an incommensurability of 1/3 is observed for other cuprate families, such as $YBa_2Cu_3O_{7-y}$ [110, 119], and therefore a universal charge order susceptibility with $\delta \approx 0.3$ has been suggested. However, in LESCO 1/8, the incommensurability does not reach 0.3 even at high temperatures. The shift towards higher values of δ could instead be influenced by soft phonons or Kohn anomalies. In this case, future ultrahigh-resolution RIXS experiments will be needed to provide a more accurate picture.

The third observation in this work is related to the temperature behaviour of the scattering amplitude and correlation length. The amplitude shows a simple power law decay of T^{-2}, which, together with the temperature evolution of the correlation length, leads to an essentially temperature-independent integrated diffraction intensity, since $I \sim \xi^2$. This means that crossing the LTT transition or the pseudogap transition has no significant impact on the integrated charge stripe order in LESCO 1/8. Thus, it can be concluded that the LTT structural transition does not trigger the charge order. In addition, the relation $I \sim \xi^2$ seems not to be restricted to LESCO 1/8, but appears to be universal among single-layer La-based cuprates. The similar crystal-field environment across these single-layer compounds justifies such a comparison of the charge order diffraction. Therefore, the low-temperature long-range correlations and integrated diffraction intensity are here shown to be similar across 1/8 doped compounds. On the other hand, the LTT onset temperature and order parameters vary between compounds, which again suggests no intrinsic link between the LTT

phase and charge order.

Another phenomenon common to LBCO, LNSCO and LESCO is a Fermi surface reconstruction reported by thermopower measurements [120, 121], which is interpreted as originating from stripe order. Furthermore, the Fermi surface reconstruction onset temperature is essentially identical among the stripe order compounds. This universality is in contrast to the difference between their in-plane correlation lengths. It seems that the integrated scattering intensity is the important parameter, not the correlation length.

4.2.4 Conclusions

The presented study on charge correlations in LESCO 1/8 illustrates how RIXS permits resonant x-ray diffraction with a well-defined energy resolution, which in turn allows elastic and inelastic contributions to be disentangled. With this technique, it can be shown that the charge-stripe correlations persist at high temperatures and appear in the absence of LTT and pseudogap phases. The emergence of charge stripe order therefore heralds a spontaneous symmetry breaking in LESCO.

Direct comparison to other single-layer stripe order compounds suggests a roughly constant integrated scattering intensity, providing a unifying picture for La-based cuprates. However, the temperature evolution of the incommensurability towards higher values raises the question of wether this is due to a connection with soft phonons or an intrinsic effect, which can only be addressed with future ultrahigh-resolution RIXS.

4.3 Fate of Charge Order in Overdoped La-Based Cuprates

Following the success of tracking the charge order to high temperatures in the 1/8-doped LESCO, the next open question to address is the evolution of charge order upon increasing the doping x. Charge order is most intense at 1/8 doping, at which it results in a suppression of the superconducting transition temperature T_C. From early measurements, it is also known that the charge order onset temperature decays when moving away from this doping value. However, the work presented in the previous section has demonstrated that more sensitive techniques are required to accurately track the evolution of charge order.

Many studies have been conducted on various cuprates to investigate the phase diagram of charge order. In $(Bi,Pb)_{2.12}Sr_{1.88}CuO_{6+\delta}$, for example, a long-range charge order has been found in the overdoped regime outside the pseudogap phase, extending almost all the way up to room temperature [122]. Even when focusing on the La-based cuprates studied in this work, different studies have reached different conclusions. Since, in $La_{2-x}Sr_xCuO_4$ and related compounds, the spin and charge order are coupled at 1/8 doping, the evolution of stripe order involves both spin and charge, unless a decoupling happens at a certain doping. Concerning the spin, a recent study on $La_{1.6-x}Nd_{0.4}Sr_xCuO_4$ reported spin-stripe order across doping values covering the whole superconducting dome [111]. On the charge side, long-range order has been suggested outside the pseudogap phase into the overdoped regime [123, 124]. By contrast, a resonant x-ray scattering study has reported two types of charge order, long-range and short-range. The long-range order is only observed near 1/8 doping and at low temperatures, whereas the short-range correlations exist at higher temperatures, but confined within the doping extension of the pseudogap phase [125]. These contradictory observations call for a systematic study on weaker charge correlations in the overdoped regime, to settle the questions about both the coupling between spin and charge, and a possible connection between charge order and the pseudogap critical doping.

This section makes use of the sensitivity of RIXS, as used to separate elastic from inelastic contributions in the previous section, to trace charge correlations as the doping is increased beyond optimal doping and the pseudogap critical doping [99].

4.3.1 Methods

The same technique was used for both the growth and preparation of the single-crystal samples as described in section 4.2.1. The RIXS measurements were conducted at the ADRESS and ID32 beamlines, where fixed angles of 130° and 149.5° between incident and scattered light were used, respectively. As before, only in-plane momentum transfer is considered because of the two-dimensional character of the crystals. The longitudinal and transverse momenta of the wave vector $\boldsymbol{q} = (h \cdot 2\pi/a, k \cdot 2\pi/b, l \cdot 2\pi/c)$ are accessed by varying the incident light angle θ and azimuth angle ϕ. Again, tetragonal notation is adopted, with $a \approx b \approx 3.79\,\text{Å}$ and $c \approx 13.1\,\text{Å}$ for LSCO. The energy and momentum resolutions are 122-129 meV FWHM and ~ 0.006 r.l.u. for ADRESS data and 33 meV FWHM and ~ 0.01 r.l.u. for ID32 data. To determine the zero energy-loss position in the RIXS spectra, the low-energy part of each spectrum was fitted with Gaussian profiles for elastic scattering and phonon excitation, with widths set by the energy resolution, a damped harmonic oscillator response function to model the magnetic excitations, and a quadratic background. Each spectrum

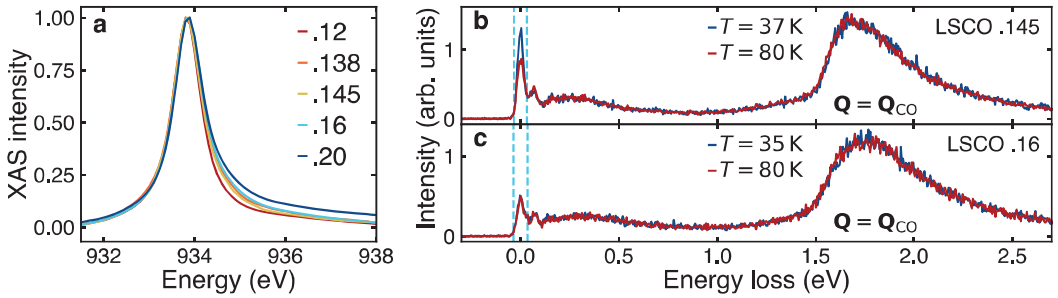

Figure 4.6: XAS and RIXS spectra of $La_{2-x}Sr_xCuO_4$. **a** Example XAS spectra of $La_{2-x}Sr_xCuO_4$ with different doping x as indicated. **b, c** High-resolution raw RIXS spectra recorded at the charge order wave vector for two different dopings and temperatures as indicated. Light blue vertical dashed lines mark the energy window for the elastic intensity integration. Figure adapted from Ref. [99].

was normalized to the integrated weight of the *dd* excitations. Analogously to the previous section, the quasi-elastic scattering was extracted from each spectrum by integrating the RIXS intensity in an energy window defined by ± FWHM around zero energy loss. From the elastic scans, a linear background was subtracted. In this fashion, longitudinal h and projected transverse k scans through the charge order wave vector were carried out for LSCO ($x = 0.12, 0.138, 0.145, 0.16, 0.2$) and LESCO ($x = 0.125, 0.21$). The base temperatures for the experiments were in the range of $\sim$ 15-25 K.

4.3.2 Results

This study was performed at the Cu L_3-edge, and example XAS spectra are shown in Fig. 4.6a for different hole dopings x. The width of the resonance peak is shown to increase with doping, consistent with previous reports [126]. The spectra also show comparable data quality that is irrespective of the doping extent. Raw RIXS spectra recorded at this resonance are shown in Fig. 4.6b and c for two different dopings $x = 0.145$ and 0.16 around optimal doping, respectively. The spectra were recorded at the charge order wave vector for high and low temperatures, as indicated. Overall, the spectra show different contributions from elastic scattering, phonon, spin and *dd* excitations at 0, 0.07, 0.3 and 1.8 eV, respectively. Importantly, the spectra show that for $x = 0.145$, the elastic scattering is prominently enhanced at lower temperatures, whereas for $x = 0.16$, no significant change can be seen.

Before discussing the doping evolution of the elastic scattering in detail, the importance of a high energy resolution is established using the raw RIXS spectra compared in Fig. 4.7 for LSCO $x = 0.145$ and 0.16, along longitudinal h and projected trans-

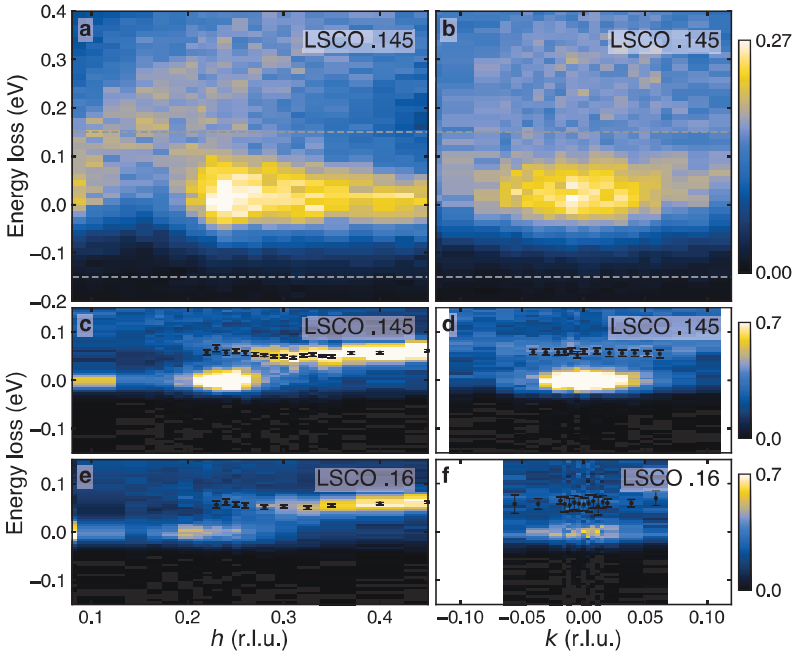

Figure 4.7: RIXS spectra of $La_{2-x}Sr_xCuO_4$ as a function of momentum. **a, b** Longitudinal h and transverse k scans recorded with an energy resolution of 129 meV. **c-f** Longitudinal h and transverse k scans recorded at a high-resolution beamline with a total energy resolution of 33 meV. Horizontal dashed lines in **a, b** illustrate the energy range in **c-f**. Black data points show the phonon dispersion. Error bars are set by the standard deviation from the fitting. Figure adapted from Ref. [99].

verse k directions. The top panels show spectra recorded with an energy resolution of 129 meV FWHM, whereas in the middle and lower panels, the energy resolution is 33 meV. The direct comparison of the same data recorded with different energy resolutions in Fig. 4.7a and c shows clearly how the quasi-elastic scattering in panel a includes both charge order and phonon scattering. This leads to a very broad peak extending to higher momentum transfers, since the charge order and phonon intensities are comparable. They can only be distinguished by applying sufficiently high energy resolution, as shown in panel c. Thus, the separation of elastic and inelastic processes is demonstrated to be vital in the study of charge correlations at higher doping levels. Again, it can be seen that the elastic scattering is reduced at $x = 0.16$, whereas the phonon intensity is comparable for the two dopings; see panels c and e. The extracted optical phonon mode dispersion in panels c-f is consistent with previous studies [123].

Having established the importance of the high energy resolution, the doping dependence is inferred by analysing the raw RIXS spectra as described in section 4.3.1

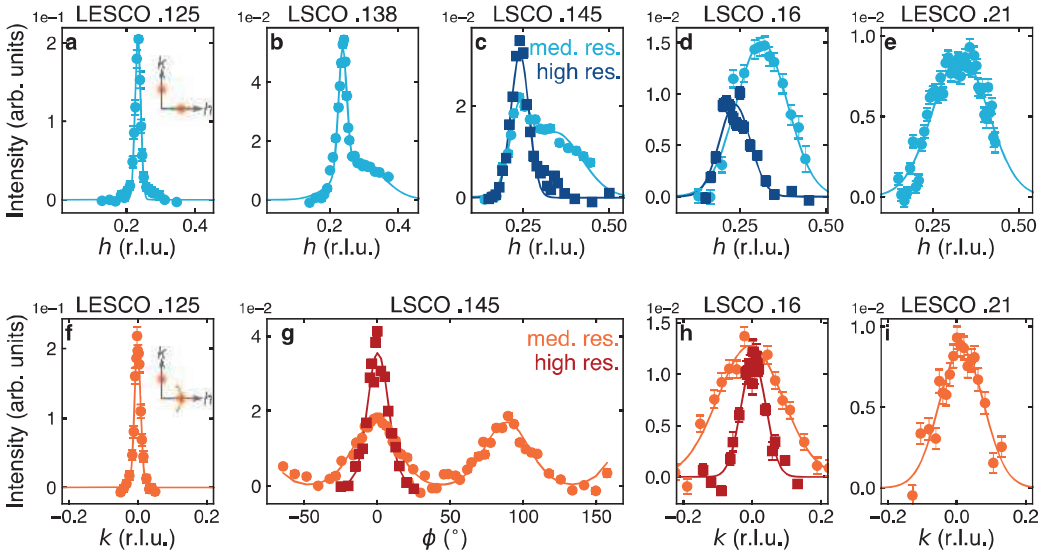

Figure 4.8: Doping evolution of the charge order. **a-e** Longitudinal h scans for the indicated compounds and doping levels. **f, h, i** Transverse k scans through the charge order longitudinal peak position for compounds and doping levels as indicated. **g** Circular arc scan through the charge order reflections with $\phi = 0$ at $(h, 0)$. Solid lines are Gaussian fits and the error bars are set by counting statistics. Insets show sketches of the charge order reflections in reciprocal space and the scan trajectories. Figure adapted from Ref. [99].

to extract elastic scans along the h and k directions. Different dopings for both LSCO and LESCO were analysed in this fashion; the doping evolution is shown in Fig. 4.8.

As seen in the previous section, charge order at 1/8 doping results in a strong and sharp reflection peak at $(\delta, 0)$ with $\delta = 0.233$. On the other hand, both at optimal doping ($x \approx 0.16$) and in the overdoped regime, the reflection peak is an order of magnitude less intense and much broader. In between 1/8 and optimal doping, the medium-resolution scans show a double peak structure in Fig. 4.8b and c. This is the convolution of charge order and phonon scattering, as discussed previously. The peak on the right at $h \approx 1/3$ stems from the optical phonon mode, which is suppressed at larger h because of absorption effects. For the transverse scans, the phonon contribution leads to a broadening of the peak. In the scans recorded with high resolution, it was possible to filter out the second peak in the h scans and the k scans appear sharper. Without sufficient energy resolution, the charge order can be misinterpreted as having a higher incommensurability and lower correlation length, or being composed of two different charge order reflections at different incommensurabilities.

Overall, the charge order reflection gradually decreases in intensity when the doping is

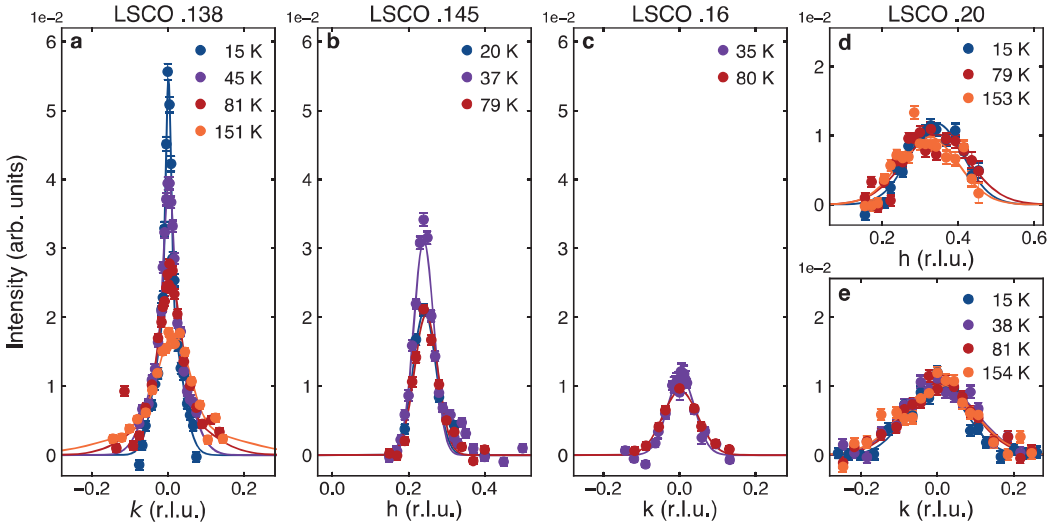

Figure 4.9: Temperature evolution of the charge order. **a-e** Elastic scans through the charge order wave vector $(\delta, 0)$ recorded at different temperatures for doping levels as indicated. Data in **b, c** were recorded with high energy resolution. Solid lines are Gaussian fits and the error bars are set by counting statistics. Figure adapted from Ref. [99].

increased, and the peak persists up to the highest doping levels measured. However, when the temperature dependence in Fig. 4.9 is taken into account, a distinct transition in the nature of the charge correlations can be observed.

Below optimal doping $x < 0.15$, represented by LSCO $x = 0.138$ and 0.145, the charge order peak shows a pronounced temperature dependence. The intensity gradually decreases for $T > T_C$, consistent with the observation in the previous section for LESCO 1/8. Interestingly, for $x = 0.145$, the intensity is also partially suppressed inside the superconducting phase $T < T_C$, represented by the 20 K data points. This is consistent with a competition between the charge order and the superconducting phase, with the latter strongest at optimal doping [125, 127].

Above optimal doping $x > 0.15$, no temperature dependence can be observed, at least up to 150 K, for either $x = 0.16$ or 0.20. The data in Fig. 4.9c-d were recorded with different energy resolutions, but from Fig. 4.7 and Fig. 4.8h, it can be observed that the higher resolution in the k scan only leads to a reduced peak width, while the intensity is essentially the same. Furthermore, if the higher resolution leads to a change in intensity, it can be assumed that this change is independent of temperature, since it is caused by the instrumentation, and not by an intrinsic temperature-dependent mechanism. Additionally, the RIXS phonon intensity shows no doping dependence for $x = 0.12$-0.21 [123], which leads to the conclusion that even if the medium-resolution measurements are capturing a signal from the phonon mode,

the temperature dependence is not influenced by it. Therefore, the absence of any temperature dependence in Fig. 4.9 can be interpreted as an absence of temperature dependence for the charge order scattering. The charge order at high doping seems to be insensitive to phase competition with superconductivity and persists up to the highest temperatures.

Altogether, the observations presented here suggest a picture of two types of charge order: a long-range order that decays with temperature above the superconducting onset temperature, and short-range temperature-independent correlations at higher doping; see Fig. 4.10d. The transition between the two can be narrowed down to a doping value between $x = 0.145$ and 0.16. This transition might even happen through a quantum critical point at optimal doping $x \approx 0.15$.

The charge order parameters (incommensurability δ, correlation length ξ and integrated intensity I/ξ^2) extracted from the elastic longitudinal scans are shown in Fig. 4.10a-c. As the doping x increases towards $\rightarrow 0.15$, the incommensurability increases slightly towards 1/4, whereas the correlation length decreases rather steeply. The integrated intensity I/ξ^2, on the other hand, stays roughly constant, as has been seen for LESCO in the previous section. Beyond the critical doping $x = 0.15$, the short-range charge correlations have similar integrated weight and incommensurability, whereas their correlation length of $\sim 10\,\text{Å}$ corresponds to around three in-plane lattice parameters.

4.3.3 Interpretation and Discussion

Several previous studies of charge stripe order in LSCO paint mutually inconsistent pictures in the overdoped region of the phase diagram. As discussed earlier, two types of charge orders in LSCO were suggested by an elastic resonant scattering study, in which long-range order was found to only exist around 1/8 doping and at low temperatures within the superconducting dome, but short-range correlations were observed at higher temperatures and up to the pseudogap critical doping [125]. In contrast, another resonant elastic study on LESCO found pronounced charge order with a temperature-independent integrated intensity up to $x = 0.20$ [128]. Further studies performed with RIXS have suggested the existence of long-range static stripe order in LSCO even outside the pseudogap regime [123, 124]. Thus, the evolution of the charge order remains elusive.

The comprehensive and systematic RIXS study of charge order presented here demonstrates long-range stripe order around 1/8 doping that decays quickly as $x \rightarrow 0.15$. Short-range correlations, however, persist at low temperatures for $x > 0.15$. This is in contrast to the recent RIXS study in which long-range order has been

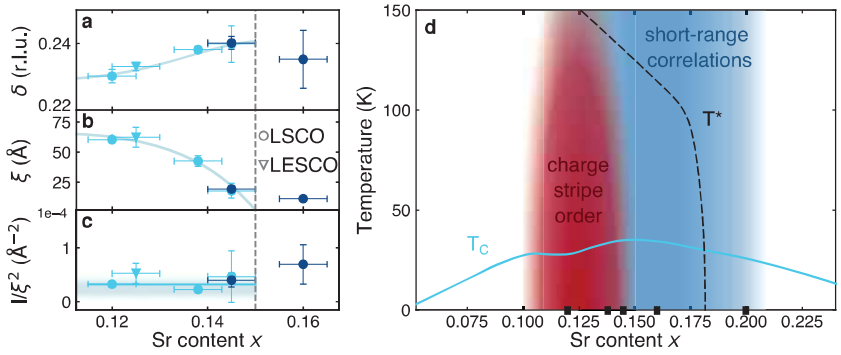

Figure 4.10: Charge order parameters and phase diagram. **a-c** Charge order incommensurability δ, correlation length ξ and integrated diffraction intensity I/ξ^2 as a function of hole doping x at base temperature. Data shown in light blue were recorded with medium energy resolution, and those shown in dark blue with high resolution. Error bars reflect the standard deviation from fitting. All coloured lines are guides to the eye. The vertical dashed line marks the doping that separates long- from short-range charge correlations. **d** Schematic charge order phase diagram showing the long-range temperature-dependent charge stripe order and the short-range temperature-independent charge correlations. The superconducting and pseudogap onset temperatures are indicated by solid light blue and dashed black lines, respectively [103, 125, 127]. Black rectangles indicate the doping levels of LSCO studied in this work. Figure adapted from Ref. [99].

observed for $x = 0.21$ [123], even though the same measurement technique was used. The picture of two types of charge order reported here, long- and short-range, is more in accordance with the elastic resonant study in Ref. [125]. However, there are pronounced differences. First, the elastic study did not record any signal from charge correlations at $x = 0.18$, and concluded that the charge order ends at the pseudogap critical doping, whereas the better sensitivity of RIXS traces the correlations up to at least $x = 0.20$, outside the pseudogap phase. Second, the elastic study reports that the end of the long-range order is under $x = 0.135$. Here, in contrast, the transition between long- and short-range order can be narrowed down to a doping range between $x = 0.145$ and 0.16, around optimal doping. Thus, with the new insights, it can be concluded that neither the short- nor the long-range charge correlations connect with the pseudogap phase and its critical doping. It has been suggested that, at this critical doping, a symmetry-breaking Fermi surface transformation takes place [129]. This transformation can, however, not be explained by the persistent short-range charge correlations, as these correlations show no change at the critical doping and are unlikely to have a strong enough impact on the electronic structure to cause a Fermi surface transformation.

The picture of charge order presented here allows for different interpretations. For the long-range temperature-dependent correlations, the prevailing view is the one

of static charge stripe order. Now the question remains wether the short-range correlations are also static or of a dynamic nature, i.e. are charge fluctuations. If they are static and the transformation goes simply from long- to short-range, the phenomenon is described by a crossover scenario. However, if they are dynamic, this implies that the static long-range order emerges through a quantum phase transition, originating in a quantum critical point. In fact, recent high-resolution O K-edge RIXS experiments suggest a dynamic nature of the correlations and therefore favour the quantum-critical scenario [130]. To confirm this, even higher energy resolution experiments may be needed. Alternatively, it may be possible to confirm the quantum critical scenario by inducing long-range order with an external tuning parameter, such as a magnetic field or hydrostatic pressure.

In general, it is conceivable that the short-range correlations originate from dynamic charge fluctuations, possibly due to electron–phonon coupling of a low-energy phonon branch. It has already been shown that there is strong electron–phonon coupling at a low-energy phonon branch around $h = 1/4$ in optimally doped LSCO [130]. The fact that the long- and short-range ordering vectors are so well aligned also hints towards a common link between the two.

Overall, this picture strongly resembles what has been found in other cuprate families, namely $YBa_2Cu_3O_{7-x}$ (YBCO) and $Nd_{1+x}Ba_{2-x}Cu_3O_{7-\delta}$ (NBCO). In these compounds, short-range correlations from quasi-elastic scattering processes have been reported and interpreted as dynamical charge density fluctuations [109, 131].The short- and long-range correlations in these compounds also appear with similar ordering vectors. However, the value of $\boldsymbol{q}_{\mathrm{CO}} = (1/3, 0)$ is distinct from that of LSCO. The origin of the different long-range incommensurabilities has yet to be settled. A possible scenario is that a different crystal structure results in a different electron–phonon coupling, which in turn generates a different lock-in mechanism for charge correlations [132]. It remains to be experimentally determined how the electron–phonon coupling assists in the formation of charge order.

In addition to the different ordering vectors, the doping dependence of the incommensurabilities differs between LSCO and YBCO/NBCO. While in LSCO, the incommensurability increases with increasing doping, the opposite trend is observed for YBCO and NBCO. If electron–phonon coupling is the sole driver of charge order, this difference would not be expected. Another parameter that can play a role is the electron–electron coupling, which is in line with many experimental studies suggesting a strong coupling picture. It remains to be seen to which extent the two interactions are responsible for the observed charge order phenomena.

Here, the short-range charge correlations have been traced up to $x = 0.20$. Regardless of the origin of these correlations, their fate in the heavily overdoped regime was

not explored. However, a recent study published after the work presented here has followed up on this point. Li *et al.* [133] report charge order in heavily overdoped LSCO thin films with $0.35 \leq x \leq 0.6$. Interestingly, this charge order shows an incommensurability of 0.165 and a large correlation length of ~ 20 lattice units. This suggests a completely different nature from the 1/8 long-range order or the short-range correlations reported here. The only similarity to the short-range correlations above optimal doping is the temperature independence. The charge order in heavily overdoped LSCO is reported to persist up to 300 K. The discovery of this charge order outside the superconducting dome opens new questions on its significance in the phase diagram and the possible connection to superconductivity. Future measurements will need to explore the overdoped region, clarifying the onset of this new charge order and its connection to the surrounding phase.

4.3.4 Conclusions

The phase diagram of charge order in La-based cuprate superconductors, as well as its connection to the surrounding phases, has long been debated. A step forward can be made by high-resolution resonant inelastic scattering studies, since they offer the required sensitivity to the valence charge density. In this section, a comprehensive RIXS study has been presented to track the fate of charge order in the overdoped limit. It was demonstrated that the long-range temperature-dependent charge stripe order is only present for $x < 0.15$ and is strongly doping-dependent, while short-range temperature-independent charge correlations persist up to the highest doping levels measured and show no doping dependence. Therefore, a more complete picture of the charge order phase can be drawn, showing that the long-range order ends around the optimal doping for superconductivity. Together with the persistence of the short-range correlations outside the pseudogap phase, it can be concluded that neither long- nor short-range correlations are connected to the pseudogap phenomenon.

The observation of long- and short-range charge correlations in LSCO is consistent with what has been reported on YBCO and NBCO, providing a unifying picture for charge order in cuprates. The long-range order seems to vanish around optimal doping, opening up the possibility that critical fluctuations play a role in superconductivity and strange metal properties.

However, the difference in incommensurability and its doping dependence leaves open the question of wether there is a different lock-in mechanism. The possible role of the electron–phonon coupling has yet to be confirmed, as well as the potentially dynamic nature of the short-range correlations.

4.4 Charge Order Lock-in by Electron–Phonon Coupling in $La_{1.675}Eu_{0.2}Sr_{0.125}CuO_4$

In the discussion of the previous section the question was raised as to what extent charge order originates from electron–electron or electron–phonon interactions. This is a difficult question to address, since strong correlations lead to a coupling of charge, spin and lattice degrees of freedom. Early theories suggested that the charge order found at 1/8 doping originates from strong electronic interactions, namely a competition between magnetic and kinetic energy resulting in doped holes forming charged stripes [108, 134, 135]. On the other hand, a momentum-dependent electron–phonon coupling can result in charge order too [136]. In both cases, the charge modulation is coupled to the lattice, which makes the distinction difficult. Furthermore, the extraction of the momentum-dependent electron–phonon coupling (EPC) strength is not an easy task, since it often relies on assumptions for the bare phononic dispersion.

Another obstacle is the sensitivity to crystalline structural changes. As shown in the first section of this chapter, charge order is especially pronounced in cuprates with an LTT structure. This suggests that the LTT phase may enhance the coupling to the electronic stripes, but a defined relation between the crystal structure and the electron–phonon interaction remains elusive.

With this background, an ultrahigh-resolution RIXS study of LESCO 1/8 is presented here, focusing on the optical phonon branch to extract its dispersion, lifetime and EPC simultaneously [93]. This is possible since the RIXS phonon scattering cross section is directly proportional to the EPC [13, 23, 24, 137].

4.4.1 Methods

High-quality single crystals of LESCO were grown and prepared in the same manner as in the previous studies. The RIXS experiments were carried out at the I21 beamline, using grazing exit geometry with linear vertical (LV) polarized light tuned to the Cu L_3 resonance at 932.5 eV. The scattering angle at I21 was fixed to 154° and the total energy resolution was 45 meV FWHM. The same convention of indicating reciprocal space in tetragonal notation was used as for the previous studies. As before, the RIXS intensities were normalized to the integrated weight of the *dd* excitations.

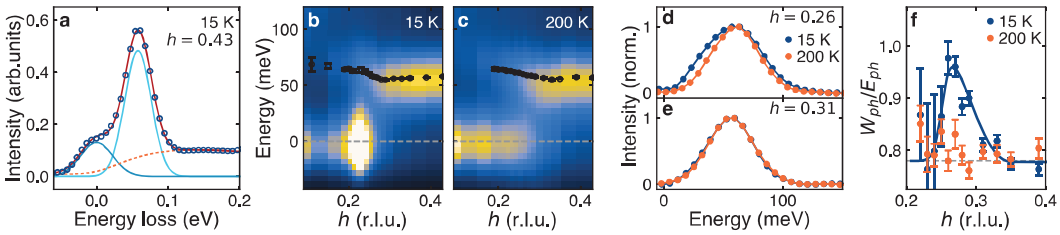

Figure 4.11: Bond-stretching phonon mode in $La_{1.675}Eu_{0.2}Sr_{0.125}CuO_4$. **a** Example RIXS spectrum focusing on low energies. The solid blue, light blue and dashed orange lines represent elastic, phonon and background contributions. The red solid line shows the total fit. **b, c** RIXS intensity distribution maps at low and high temperatures. Black data points represent the phonon dispersion extracted from fitting. Error bars are set by the standard deviation. To avoid the overwhelming elastic scattering from charge order, the data at 15 K were recorded along $\boldsymbol{q} = (h, h\tan\phi)$ with $\phi = 4°$. **d, e** RIXS spectra with elastic and background contributions subtracted. **f** Parameter W_{ph}/E_{ph} as a function of h. Solid lines are guides to the eye. Figure adapted from Ref. [93].

4.4.2 Results

The example RIXS spectrum in Fig. 4.11a shows a pronounced phonon excitation peak around 60 meV dominating over elastic and paramagnon scattering contributions. This phonon excitation can be assigned to the in-plane copper–oxygen bond-stretching phonon, consistent with previous inelastic neutron scattering [138], inelastic x-ray scattering [139] and RIXS studies [118, 123]. To infer the momentum dependence of this phonon mode, RIXS spectra were taken for varying in-plane momentum transfer h, as shown in Fig. 4.11b and c for two different temperatures. As seen in a previous section, charge stripe order is suppressed by a factor of two by increasing the temperature from 15 K to 200 K.

The phonon mode is extracted from the spectra by fitting with three different components: a Gaussian profile for elastic scattering, another Gaussian for the phonon mode, and a damped harmonic oscillator function convoluted with the insturmental resolution for paramagnon-dominated background. With this routine, the phonon can be isolated from the spectra by subtracting elastic and background contributions. This is shown in Fig. 4.11d and e for different wave vectors and temperatures. One can infer that, at high temperatures, the phonon linewidth is resolution-limited for both wave vectors. At low temperatures, on the other hand, the linewidth shows a weak but significant enhancement at $\boldsymbol{q}_{\mathrm{CO}}$, indicating a decrease in the phonon lifetime. From the phonon mode, the dispersion E_{ph}, its linewidth W_{ph} and the relative EPC strength can be extracted.

Figure 4.11f shows how the dimensionless parameter W_{ph}/E_{ph} is essentially featureless

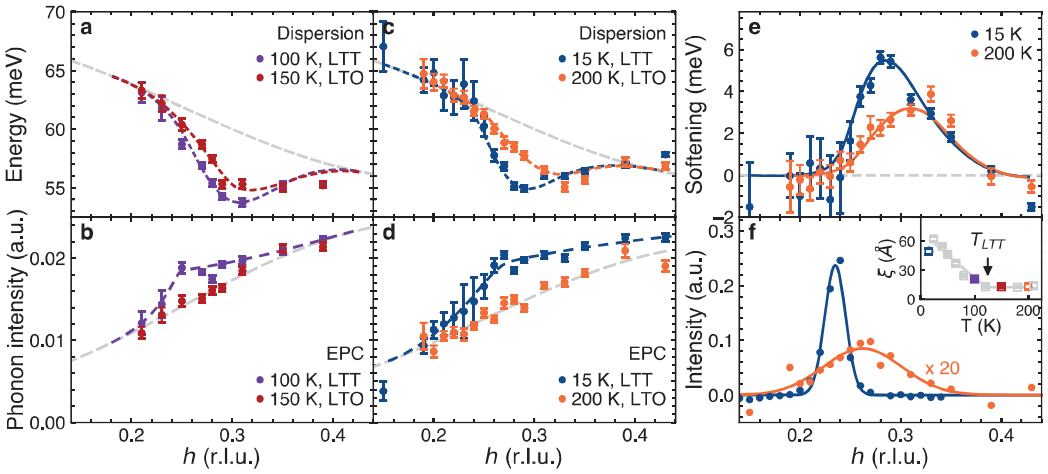

Figure 4.12: Temperature evolution of the phonon anomaly. **a, c** Phonon dispersion and **b, d** integrated spectral weight along the in-plane longitudinal direction across $\boldsymbol{q}_{\mathrm{CO}}$ for different temperatures. Grey dashed lines in **a, c** and **b, d** are the DFT bare bond-stretching phonon dispersion and the phonon spectral weight above the LTT temperature fitted to a $\sin^2(\pi h)$ function, respectively. **e** Softening of the excitation energy extracted from **c** for two different temperatures. **f** Charge order peak obtained by integrating elastic intensities over −45-30 meV. Solid lines are Gaussian fits. The inset shows the charge order correlation length ξ as a function of temperature. Open square data are from Ref. [98]. Figure adapted from Ref. [93].

at high temperatures across $\boldsymbol{q}_{\mathrm{CO}}$. At low temperatures, by contrast, the increase in linewidth combined with a softening of the phonon dispersion results in a 20% increase in W_{ph}/E_{ph} around $\boldsymbol{q}_{\mathrm{CO}}$.

To gain insight into the variation of the phonon parameters with momentum, the phonon dispersion and spectral weight, which is proportional to the EPC strength, are shown in Fig. 4.12 for different temperatures in the LTT phase and the LTO phase above it. From density functional theory (DFT) calculations [140, 141], the bond-stretching phonon mode energy is expected to disperse monotonically downwards from the zone centre towards higher momentum; see the grey dashed lines in Fig. 4.12a and c. However, the experimentally observed phonon softening around the charge order is much stronger than predicted by DFT and more pronounced for low temperatures. The softening magnitude is obtained by subtracting the bare phonon dispersion from the experimental data and is displayed in Fig. 4.12e. The maximum value of ~ 5 meV is observed at 15 K. Interestingly, the maximum is shifted to lower h values compared to the 200 K data. This resembles the behaviour of the charge order peak, as shown in panel f. However, the phonon softening occurs at slightly higher values of h compared to the charge order incommensurability.

Next, the evolution of the EPC strength as expressed by the integrated phonon intensity in RIXS is discussed. As explained in section 2.1, phonons are excited in the RIXS scattering process via the EPC in the intermediate state with an extra valence electron and a core hole. It is intuitive that the stronger the coupling between electron and lattice, the stronger the phonon signal measured by RIXS. In addition, the longer the core-hole lifetime ($1/\Gamma$), the longer the time the lattice has to react to the different charge density in the intermediate state. This means that the phonon signal is intuitively also inversely proportional to Γ. The theory behind the phonon signal and the EPC was introduced by Ament *et al.* [23], and its application to cuprate RIXS spectra was thoroughly investigated by Braichovich *et al.* [24]. The theory is based on localized electrons and Einstein (non-dispersive) phonons and derives an exact expression for the scattering amplitude from a Hamiltonian consisting of a phonon part and an electron–phonon coupling part, to calculate the RIXS cross section [23]. From this, the one-phonon and multi-phonon intensities can be derived. The resulting phonon intensity shows a universal dependence on the ratio EPC/Γ [24], as intuitively described above for small EPC. A detailed analysis shows that there are three different ways of extracting the EPC from RIXS spectra. First, the ratio of the one-phonon and two-phonon intensities, together with the phonon energy and core-hole lifetime, can give an absolute value of the EPC within the described framework, since the ratio of intensities eliminates the need to know an absolute instrument efficiency. Second, the EPC can be extracted from the measurement of the one-phonon intensity as a function of the detuning of the incident photon energy from the resonance. Third, the one-phonon intensity on resonance can give the absolute EPC if one knows the absolute value of intensity. Here, the third method is used without absolute intensity values to give the relative EPC as a function of momentum and temperature. As will be shown below, conclusions can be made about the momentum-dependent EPC in connection with charge order without deriving the absolute EPC.

Looking at the phonon intensity in Fig. 4.12b and d, a pronounced difference can be observed when comparing the 100 K below the LTT onset to the 150 K data above. In the LTO phase, the EPC strength increases slowly and monotonically with momentum h, whereas in the LTT phase, the phonon weight is significantly enhanced around $\boldsymbol{q}_{\mathrm{CO}}$. This behaviour is further enhanced upon cooling to low temperatures, as shown in panel d. From these data, it can therefore be inferred that the EPC is amplified in the LTT phase around the charge order wave vector. This effect is summarized in Fig. 4.13, which shows the dispersion as well as the EPC strength anomaly.

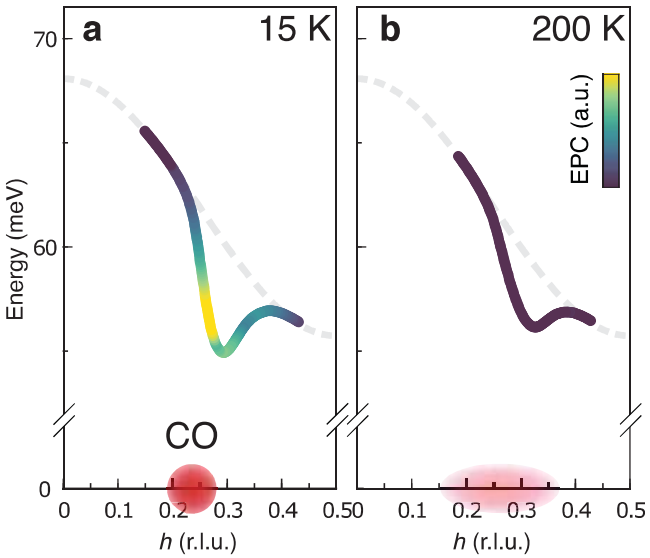

Figure 4.13: Momentum dependence of the EPC and charge order. **a** Low-temperature and **b** high-temperature schematic of the soft bond-stretching phonon mode and the charge order. The red point around $\boldsymbol{q}_{\mathrm{CO}}$ indicates the charge order width. the coloured line is the measured phonon dispersion, and the grey dashed line represents the dispersion calculated using DFT. The colour indicate the enhancement of the EPC strength above the expected $\sin^2(\pi h)$ momentum dependence. Figure adapted from Ref. [93].

4.4.3 Interpretation and Discussion

First, the phonon anomaly as a softening of the phonon energy is discussed. Several different mechanisms can cause such a softening effect. One possibility is the conventional Kohn anomaly, which results from a Fermi surface nesting leading to a charge density wave [136]. However, this anomaly is expected to be a sharp dispersion dip, whereas the results here show a softening over a broad momentum range of 0.23-0.4 r.l.u. Another interpretation is a Fano resonance of the charge excitation that interferes with optical phonons. This phenomenon was used to explain data on Bi-based cuprates [142, 143]. There, the phonon softening exceeds what is expected for an EPC effect and, additionally, the phonon intensity increases nonmonotonically with momentum. This behaviour is not observed here, where the softening magnitude is in accordance with typical phonon self-energy effects and where the intensity enhancement is still in accordance with a monotonic dependence. In fact, the enhanced intensity around $\boldsymbol{q}_{\mathrm{CO}}$ is still smaller compared to the intensity near the zone boundary. It cannot be ruled out that both Fano resonance and EPC are involved in the phonon anomaly in LESCO, but the significantly smaller softening and intensity enhancement compared to the Bi-based compounds suggest that the dominant effect comes from EPC.

The link between the phonon anomaly and charge order is difficult to establish. There is no direct proportionality between the two, and the softening is already established at temperatures where there is no long-range charge order; see Fig. 4.12c and f. At lower temperatures, the charge order is enhanced by an order of magnitude, whereas the softening only changes marginally. However, the broad momentum width of the softening resembles the short-range charge correlations at high temperatures. This suggests a strong coupling between the short-range charge fluctuations and the bond-stretching phonon mode.

The momentum dependence of the EPC strength reported in Fig. 4.12b and d reveals the main observation of this study. While the momentum dependence above the LTT onset temperature follows the expected $\sin^2(\pi h)$ behaviour, as is observed for other cuprate systems [123], the trend changes upon cooling into the LTT phase. A pronounced enhancement is detected around the charge order wave vector. This suggests that the EPC is enhanced in the LTT phase around $\boldsymbol{q}_{\mathrm{CO}}$. Notably, this enhancement is not observed in LSCO 1/8, which also does not have an LTT phase. An explanation for this is that, in the absence of an LTT lattice distortion, there is a mismatch between the copper–oxygen bond and the average stripe directions [144]. This reduces the coupling between the charge correlations and the phonon modes.

Altogether, this study reveals that the EPC of the bond-stretching phonon mode in LESCO 1/8 is enhanced at $\boldsymbol{q}_{\mathrm{CO}}$ only in the LTT phase. At the same time, the charge order correlation length gradually increases below the LTT onset temperature; see the inset of Fig. 4.12f. Thus, the link between the LTT, EPC and charge correlations suggests that the EPC promotes long-range charge order formation. In the first section of this chapter, it has been shown that short-range charge correlations form spontaneously at high temperatures above the LTT onset, and that the integrated weight of the charge order is essentially independent of temperature and thus not linked to the LTT phase. With the new insights presented here, it can be concluded that, while charge order is not intrinsically linked to the LTT structure, the enhancement of EPC inside the LTT phase triggers a lock-in of charge modulations at a specific ordering wave vector, promoting the long-range charge order formation. This can be explained by the fact that in LESCO, the LTT distortion has the same symmetry-breaking tendency as the stripe order. Therefore, the lattice modulation may enhance the coupling to the electronic degree of freedom and stabilize the stripe order. However, it remains unclear if the enhanced EPC is a cause or a result of long-range charge order. Furthermore, the mismatch of the exact momentum of the phonon softening and peak in EPC with $\boldsymbol{q}_{\mathrm{CO}}$ may indicate a combined effect of electronic correlations and EPC, which together define the charge order.

When the RIXS energy resolution can be improved further in the future, it may become possible to study lower phonon modes too, e.g. the buckling mode. Such

studies could investigate all phonon modes that are potentially relevant to the charge order and infer their momentum-dependent EPC strengths. This would offer a comprehensive understanding of their underlying connections and of the phonon anomalies in vicinity of charge order. For a complete picture, a systematic study of the EPC in different phonon modes as a function of doping could help in understanding the relations between different phases.

4.4.4 Conclusions

The driving interaction of charge order in cuprates has remained elusive for many decades. Both electron–electron as well as electron–phonon interactions have been proposed. The study reported here offers a deeper insight into the electron–phonon coupling in LESCO 1/8, which shows strong long-range charge order and an LTT phase. The RIXS results on the in-plane bond-stretching phonon mode show a broad softening in momentum space and an enhancement of the EPC strength around $\boldsymbol{q}_{\mathrm{CO}}$ only inside the LTT phase. This suggests that the LTT lattice structure enables a momentum-dependent EPC. This EPC enhancement then triggers a lock-in of the charge stripes and promotes long-range charge correlations.

The study highlights the importance of the electron–phonon interaction for long-range charge order in LESCO, and possibly other cuprates. Furthermore, the substantial momentum-dependent EPC of the bond-stretching phonon mode may have important implications for the long-debated role of phonons in the unconventional superconductivity in cuprates.

5 Electronic Structure of the Spinel Superconductor $LiTi_2O_4$

In addition to the archetypal model systems, the ruthenates and cuprates that have been studied extensively over many decades and in the previous two chapters, many other correlated electron systems show an emergence of various quantum phases. This chapter focuses on the only spinel oxide superconductor, $LiTi_2O_4$, which was discovered in the early 1970s and has a transition temperature $T_C \approx 11\,\mathrm{K}$ that was considered relatively high at the time [145]. This superconductor is of great interest because of its proposed applications as a battery material or a transparent superconductor in optoelectronic devices [146, 147]. However, insight into the microscopic mechanisms has been hindered by the high sensitivity of $LiTi_2O_4$, which is prone to dissipate Li atoms, resulting in a change in its superconducting properties [148]. Only recently has epitaxial thin-film growth of $LiTi_2O_4$ been achieved, opening the door for a systematic investigation of its physical properties [149]. To gain an understanding of the superconducting state, knowledge of the electronic band structure is required. Here, an ARPES study of $LiTi_2O_4$ (111) thin films reveals the three-dimensional electronic band structure. The experimental data and insights are being prepared for a manuscript [150], and therefore represent work in progress. I am contributing to the manuscript by planning, preparing and leading the execution of the experiments, the analysis and interpretation of the data, and by writing the manuscript together with my supervisor, with inputs from all co-authors. Below, the debate about the superconducting mechanism in $LiTi_2O_4$ is briefly outlined, before the details of the experimental study are presented.

5.1 Superconductivity: Conventional or Anomalous?

One of the main reasons why $LiTi_2O_4$ is still studied intensively is the debate about its superconducting mechanism. Early on, it was suggested that $LiTi_2O_4$ is a medium-coupling s-wave superconductor, and indeed the superconductivity can be described by BCS theory [151]. However, more recently, new experimental data have been obtained and more anomalous superconducting mechanisms have been proposed:

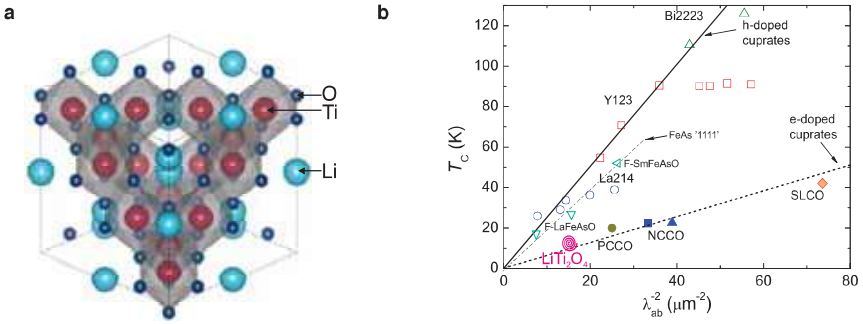

Figure 5.1: $LiTi_2O_4$. a Crystal structure of $LiTi_2O_4$. **b** Uemura plot showing the superconducting transition temperature T_C as a function of the London penetration depth λ_{ab} for electron- and hole-doped cuprates, the FeAs '1111' systems and $LiTi_2O_4$. From Ref. [157]

resonating valence bond [152, 153], bipolaronic [154] and d-wave pairing symmetry like in the cuprates [155, 156].

The crystal structure of $LiTi_2O_4$ is different from the famous two-dimensional perovskite crystal lattice in the cuprates, as it grows in the cubic spinel structure with space group $Fd\bar{3}m$, with a lattice constant of $a = 8.4$ Å; see Fig. 5.1a. The frustration in the lattice, with distorted atomic bonds, leads to a mixed valence state of Ti^{3+}, with spin $S = 1/2$, and Ti^{4+}, with $S = 0$. This results in only half an electron residing in the $3d$ t_{2g} valence energy levels of Ti. Despite the difference in the crystal lattice structure, $LiTi_2O_4$ shows several similarities to the cuprates. First, the superconducting phase is situated close to a metal-insulator transition [158]. Second, the d–d electron correlations have been found to play an important role in the electronic structure of this system [159]. Third, the mixed valence state favours short-range spin ordering, and an anomalous magnetoresistance has been interpreted as evidence of spin–orbit scattering and an orbital-related state, showing the importance of spin–orbital fluctuations in $LiTi_2O_4$, similar to cuprates. Furthermore, a scanning tunnelling microscopy study on thin films reports a pseudogap at the Fermi level modifying the surface superconductivity [160]. Additionally, low-energy muon spin rotation measurements have revealed the London penetration depth and shown that if added in the Uemura plot, $LiTi_2O_4$ falls on the line of electron-doped cuprates; see Fig. 5.1b. Even more intriguing, a recent investigation into its magnetoresistivity and upper critical field found a fourfold rotational symmetry in the superconductivity, attributed to unconventional d-wave superconducting Cooper pairs [156]. Thus, many results point towards an anomalous superconducting mechanism that seems to have many similarities with the high-T_C cuprate superconductors.

The question of the detailed superconducting mechanism remains, since evidence for anomalous superconductivity increases, and demands further experimental insights